Nanoscale

PAPER

View Article Online
View Journal | View Issue

Cite this: *Nanoscale*, 2025, **17**, 10761

Ultrasensitive electroanalytical sensing platform using aptamer-conjugated V_2CT_x MXene for the detection of the HER-2 biomarker†

Reema Rawat,[a] Sonam Singh,[b] Souradeep Roy,[a] Samarika Dubey,[c] Tapas Goswami, [b] Ashish Mathur *[d] and James McLaughlin[e]

Received 29th October 2024,
Accepted 31st March 2025

DOI: 10.1039/d4nr04503c

rsc.li/nanoscale

Breast cancer is a leading cause of mortality among women globally, with the human epidermal growth factor receptor-2 (HER-2) serving as a vital biomarker for its diagnosis and management. In this study, an electrochemical aptasensor was developed using V_2CT_x MXene for the sensitive and selective quantification of HER-2. The sensor's electrochemical performance was evaluated through cyclic voltammetry (CV) and square wave voltammetry (SWV) that demonstrated a wide linear detection range of 1 ng mL^{-1} to 100 μg mL^{-1}. The aptasensor achieved an exceptional detection limit of 0.36 ng mL^{-1} and a quantification limit of 1.96 ng mL^{-1} under optimized conditions. Furthermore, the sensor displayed excellent selectivity for HER-2 against other biomarkers and retained stability for 40 days, making it suitable for prolonged use. The high electrochemical response was attributed to the exceptional surface-to-volume ratio and conductivity of the V_2CT_x MXene, enabling efficient aptamer immobilization and signal enhancement. These findings highlight the potential of the developed aptasensor as a non-invasive, reliable, and cost-effective platform for early HER-2 detection, paving the way for improved breast cancer diagnosis and monitoring.

Introduction

Breast cancer is the most serious cancer that affects women's health and lives.[1] It ranks as the second main cause of cancer among women, contributing to 34% of all malignancies and impacting around 2.1–2.3 million people worldwide every year. In 2020, there were 2.261 million new cases of breast cancer and 0.685 million deaths worldwide. By 2025, the number of breast cancer cases in India is expected to increase to 232 000 from the current 205 000.[2] HER-2, also called ErbB-2 (avian erythroblastosis oncogene B), is overexpressed by twenty to thirty percent in breast cancer cells, making it a well-established biomarker to aid in medical supervisory for patients with breast cancer.[3] The person affected with breast cancer typically shows higher HER-2 levels (15–75 ng mL^{-1}) in blood as compared to the levels seen in healthy individuals (2–15 ng mL^{-1}).[4] Therefore, developing a quick, sensitive, label-free, and affordable method for detecting HER-2 levels is necessary.

Current diagnostic techniques, including pathological testing, mammography, sonography, thermography, magnetic resonance imaging (MRI), molecular breast imaging, positron emission tomography (PET), biopsy, and computerized tomography (CT), also known as the "gold standard" for breast cancer diagnosis, can provide scientific and reliable data.[5] However, they have the drawbacks of being time-consuming and invasive, which are not ideal for early cancer detection. The proximity between normal and cancerous cells makes diagnosing and treating breast cancer challenging.[6] Women in rural areas face numerous challenges regarding healthcare and regular checkups. The lack of healthcare facilities often leaves them unaware of symptoms indicative of conditions like breast cancer. Without regular checkups, their health can deteriorate to a critical point where the cancer becomes fatal.[7] The absence of local healthcare facilities forces many women to travel long distances to urban hospitals. Due to the distance and associated costs, many families opt for local, often inadequate, care. Additionally, societal attitudes and taboos further complicate matters, discouraging women from seeking the help they need.[8] These combined factors result in a severe lack of resources and support for women in rural areas. As a result, there is a need for different approaches, non-invasive, portable, and cost-effective screening methods that offer high sensitivity and specificity for point-of-care (POC) diagnosis.

---

[a] *Health Technology Cluster, School of Health Sciences and Technology, UPES, Dehradun, India. E-mail: ashish.mathur@ddn.upes.ac.in, nanoashish@gmail.com*
[b] *Department of Chemistry, School of Advanced Engineering, UPES, Dehradun, India*
[c] *The Tons Bridge School, Nanda ki Chowki, Premnagar, Dehradun, India*
[d] *Centre for Interdisciplinary Research and Innovation (CIDRI), UPES, Dehradun, India*
[e] *School of Engineering, Ulster University, Belfast, UK*

† Electronic supplementary information (ESI) available. See DOI: https://doi.org/10.1039/d4nr04503c

Electrochemical DNA sensing methods have been given extreme consideration due to the high specificity of DNA.[9] Using nanomaterials for signal amplification has improved the sensitivity and selectivity of DNA-based electrochemical biosensors.[10] Incorporating suitable nanomaterials as bioelectrode modifiers further enhances the electroanalytical properties of biosensors. The high surface-to-volume ratio of these nanomaterials allows for improved receptor immobilization, while their quantum confinement properties lead to enhanced electronic conductivity and increased signal amplification. These advancements have extensively benefited the development of electrochemical biosensors.[11,12] MXenes are an emerging class of 2D biomaterials that have attracted significant research interest for potential biomedical applications in biosensing, bioimaging, and cancer therapy. This interest is due to their intriguing physicochemical properties and highly variable structures and compositions.[13,14] Due to their 2D structure, these materials have an elevated surface-to-volume ratio, enhancing the availability of ion-active sites.[15] This increased number of active sites and the ability to adsorb ions can improve electrochemical performance. Additionally, tuneable surface chemistry with various functional groups, such as hydroxyl, oxygen, and fluorine, further enhances this performance.[16,17] A tuneable work function offers several advantages, including using the MXene electrode as either a hole or an electron transport layer. It also facilitates the development of strategies to enhance electrochemical stability and performance, such as tuning the interlayer structure and surface area and increasing electrode conductivity.[18]

One such type of MXene is vanadium MXene (V_2CT_x), which is widely used in developing electrochemical sensors, biosensors, gas sensors, batteries, *etc*. V_2CT_x stands out for its unique combination of electronic conductivity, mechanical flexibility, and abundant active sites provided by its surface terminations. These properties make it a promising material for biosensing applications, particularly in point-of-care diagnostics for biomarkers such as HER-2. However, to the best of our knowledge, no studies have been reported on using V_2CT_x MXene in the biosensing field.

In this study, we focused on developing an electrochemical aptasensor platform using V_2CT_x MXene for detecting breast cancer through the HER-2 biomarker, representing a novel application of this material. The high surface area and superior conductivity of the V_2CT_x MXene facilitated efficient aptamer immobilization and signal amplification, critical for achieving high sensitivity and specificity in biomarker detection. V_2CT_x nanoparticles were immobilized on carbon screen-printed electrodes (CSPE) using a drop casting technique, followed by EDC–NHS coupling. Signal amplification was accomplished through cyclic voltammetry and square wave voltammetry. The developed aptasensor demonstrated a broad linear range and high sensitivity, offering a promising method for detecting HER-2 in human serum for early breast cancer diagnosis. This innovative approach highlights the potential of the V_2CT_x MXene to transform biosensing applications and establish itself as a key material in the field of diagnostic healthcare.

Experimental section

Reagents and methods

The carbon-based screen-printed electrodes (CSPE) (1 mm diameter) were bought from Micrux Technologies, Spain. Sodium monobasic and dibasic salts (NaH_2PO_4 and Na_2HPO_4) and Methylene Blue (MB) were sourced from Fisher Scientific, India. Sodium hydroxide (NaOH), *N*-hydroxy succinimide (NHS), 1-ethyl-3-(3-dimethyl aminopropyl) carbodiimide (EDC), dimethylformamide (DMF) and acetone were bought from Merck India Pvt. Ltd. The V_2AlC MAX powder was procured from Nanoshell UK Ltd. Hydrofluoric acid (HF) and hydrochloric acid (HCl) were bought from Sigma-Aldrich. The aptamer and the recombinant fusion protein (HER-2-Fc), the protein comprising two extracellular domains of HER-2 linked to a human Fc fragment, were bought from Gene Bio Solutions in Dehradun, India. The sequences were based on those reported by Limin Chun *et al.* and were stored at −20 °C until use. Deionized (DI) water with a specific resistivity of 18.2 MΩ was utilised in every test. The aptamer sequence is provided below.

Aptamer sequence: NH2-5′-CTT CTG CCC GCC TCC TTC C-(TGG GGC CTG GAT ACG GAT TGG TAA GGA TTA GTA GGG GGC ATA GCT)-GGA GAC GAG ATA GGC GGA CACT-3′.[3]

Synthesis of V_2CT_x MXene

Vanadium carbide MXene was synthesized as described in the literature.[19] The process began by preparing an etching solution in distilled water, combining hydrofluoric acid (HF) and hydrochloric acid (HCl) in a 12 : 12 : 6 volume ratio, totalling 60 mL. Next, 2 grams of V_2AlC MAX powder were slowly added to this etching solution and stirred at 40 °C and 300 rpm for 120 hours. After the etching, the solution was repeatedly washed with distilled water until the pH reached approximately 6 and then centrifuged at 3200 rpm for 10 min. The resulting powder was then dried under vacuum at 80 °C for 24 hours, producing a greyish-black powder.

Characterization of V_2CT_x MXene

The X-ray diffraction (XRD) of the V_2CT_x MXene powder was performed using an XRD spectrometer with Cu Kα radiation (λ = 0.154 nm) at a 2θ span of 5°–80° to analyse the phase structure. Field emission-scanning electron microscopy (FE-SEM, JOEL, USA; beam energy = 10 keV) was utilised to characterize the surface of the synthesized V_2CT_x. Fourier Transform Infrared Spectroscopy (PerkinElmer FTIR Spectrometer) was performed to analyse various functional groups within 4000–400 cm^{-1}. The UV-Vis absorption spectrum of V_2CT_x was recorded using a UV-Vis spectrophotometer (LAMBDA 35, PerkinElmer). Raman spectrometry (Raman, PerkinElmer Raman spectrometer) was used to analyse the quality of V_2CT_x at wavelengths of 200–1600 cm^{-1}. Transmission Electron Microscopy (TEM, THERMO FISHER TALOS F200X) was utilized to analyze the microstructure of the synthesized material. The material's surface chemistry was analyzed using X-ray Photoelectron Spectroscopy (XPS, PHI5000 Versa Probe II, ULVAC-PHI, Japan).

Sensor surface characterization

The working area (1 mm) of a flexible electrode made from screen-printed carbon was treated with 1 μL of 1 mg mL^{-1} V_2CT_x solution and air-dried at 25 °C for 2 hours. Subsequently, the nano-enabled carbon electrode was again modified *via* immobilizing 1 μL of HER-2 aptamer through amide linkage using EDC–NHS coupling chemistry. The electrode was then incubated for 24 hours at 4 °C. This process led to developing a V_2CT_x/Aptamer-based HER-2 bio-electrode designed to detect HER-2.

Electrochemical analysis

Electrochemical analyses were conducted using a three-electrode setup with a DropSense μStat i-400 potentiostat. The V_2CT_x/Aptamer-modified carbon electrode, and two gold pads, functioned as the working, counter and reference electrodes, respectively. The electrolyte utilized was Phosphate Buffer Saline–Methylene Blue redox indicator (PBS-MB, 0.1 M/ 100 μM, pH 7). Preliminary electrochemical characterization and HER-2 detection performance of the CSPE/V_2CT_x surface was assessed *via* cyclic voltammetry (CV), spanning from 0.5 to −0.5 V at a scan speed of 100 mV s^{-1}.

The optimization of the sensor involved evaluating aptamer concentrations (10–50 μM), incubation times (1–5 min), and electrolyte pH levels (5–7.5) to enhance the aptamer recognition process. These optimizations were conducted using Square Wave Voltammetry (SWV) with a voltage range of 0.1 to −0.6 V, a scan speed of 100 mV s^{-1}, and a frequency of 20 Hz. Under the optimized conditions, SWV was further employed for analytical sensing studies. HER-2 concentrations were varied from 1 ng mL^{-1} to 100 μg mL^{-1}, with each measurement performed using a fixed sample volume of 70 μL.

Results and discussion

V_2CT_x surface characterization

The XRD pattern, as depicted in Fig. 1(a), shows that the analysis was performed on both the MAX phase (V_2AlC) and the synthesized MXene (V_2CT_x). It is evident that in the MAX phase, the peak at $2\theta = 13.3°$, corresponding to the 002 orientation, shifts to a lower angle of $2\theta = 7.8°$ in the MXene. This shift is due to the exfoliation of the aluminum layer, increasing the interlayer spacing.[20] Other peaks associated with the V_2AlC MAX phase are diminished or reduced, confirming the successful synthesis of vanadium carbide MXene. FTIR spectroscopy in Fig. 1(b) revealed various surface functional groups, such as –O/OH at 3374 cm^{-1}. Further absorption bands at 1637 cm^{-1} correspond to the C═C stretching vibration,[14] while bands at 966 cm^{-1} and 863 cm^{-1} correspond to the presence of C–O. The vibrations observed at 964 cm^{-1} and 464 cm^{-1} resemble the metal and oxygen bonding of V═O and V–O, respectively, in the as-synthesized MXene.[21] The UV-Vis spectra of the MAX phase and MXene in *N*-methyl pyrrolidone solvent in Fig. 1(c) are consistent with the literature, indicating that V_2AlC and V_2CT_x do not exhibit any absorption peaks in the visible region. However, a slight absorption curve is observed between 300 and 400 nm.[13] The calculated optical band gap from the Tauc plot is determined to be 4.2 eV, indicating a wide-band gap nature. Raman spectroscopy of the vanadium MXene depicted in Fig. 1(d) displays prominent peaks, as reported by Eunji Lee *et al.*[22] The peak at 283 cm^{-1} is typically associated with the $E1_g$ vibrational mode, which involves in-plane vibrations of V atoms within the MXene layers. The peaks at 401 cm^{-1} and 520 cm^{-1} correspond to active vibrational modes related to surface terminations[23,24] of the MXene, primarily arising due to V–O bonds and their interaction with surface terminations such as oxygen and hydroxyl groups. Furthermore, the peak at 699 cm^{-1} is attributed to the $A1_g$ vibrational mode, indicating out-of-plane vibrations of V atoms, suggesting the presence of ordered surface terminations. These assigned peaks collectively provide insights into the structural and vibrational properties of the as-synthesized V_2CT_x MXene, confirming the successful etching and termination of the MXene layers. Fig. 1(e) depicts the field emission scanning electron microscopy (FESEM) image of the synthesized V_2CT_x MXene, showing a distinct accordion-like three-dimensional morphology. The structure consists of interconnected, stacked layers with varying degrees of compaction and exfoliation. This morphology is characteristic of MXenes synthesized through the etching process, highlighting their ability to form loosely packed, multi-dimensional architectures with exposed active surfaces, facilitating enhanced material performance. The EDX spectrum in Fig. 1(f) confirms the elemental composition of the synthesized V_2CT_x MXene. The composition includes vanadium (V) at 59.91%, carbon (C) at 5.63%, oxygen (O) at 25.63%, fluorine (F) at 6.17%, and aluminum (Al) at 2.64% (atomic percentage). The significant presence of vanadium and carbon supports the successful synthesis of the MXene structure. At the same time, the oxygen and fluorine peaks indicate functional groups (–OH and –F) introduced during the etching process. The small amount of aluminum suggests partial retention from the parent V_2AlC phase.

To further investigate the morphology of the V_2CT_x MXene, TEM analysis was conducted, as depicted in Fig. 1(g). The images reveal that the 2D flake structures are stacked in a few single layers.[20] A high-resolution TEM (HR-TEM) image (Fig. 1h) highlights the lattice fringes, with an interplanar spacing measuring 0.253 nm.[25] Additionally, the selected area electron diffraction (SAED) pattern in Fig. 1(i) confirms the crystalline nature of the synthesized V_2CT_x MXene. Elemental composition analysis was performed using energy-dispersive X-ray spectroscopy (EDX) mapping, as shown in Fig. 2(j), confirming the presence of vanadium (V), carbon (C), oxygen (O), and fluorine (F).[26]

X-ray photoelectron spectroscopy (XPS) of V_2CT_x

The elemental states and chemical composition of the V_2CT_x MXene were studied through X-ray photoelectron spectroscopy (XPS) analysis. The XPS survey scan in Fig. 2(a) shows the presence of V, C, O, and F in the as-synthesized MXene. The C 1s

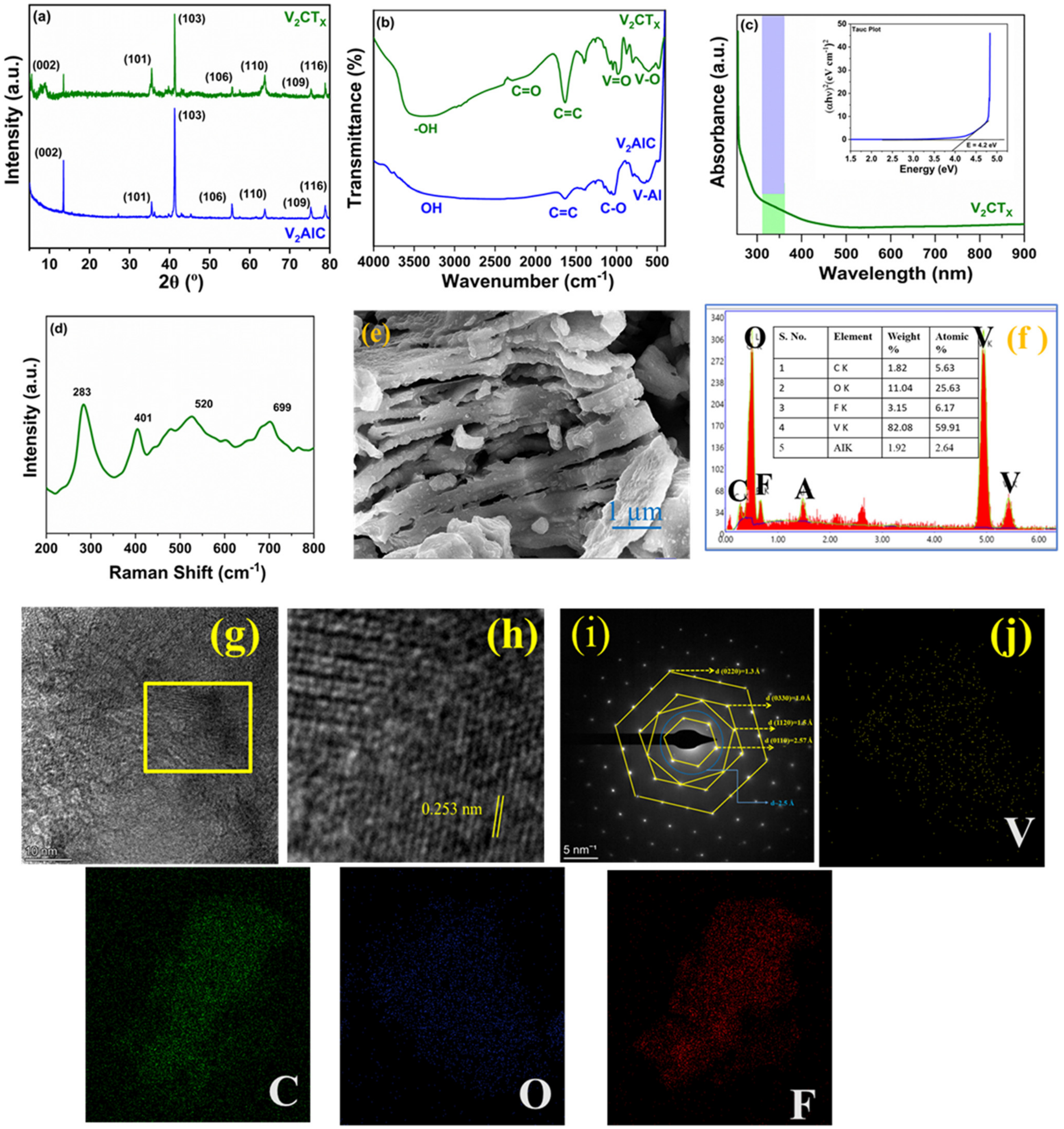

S. No.	Element	Weight %	Atomic %
1	C K	1.82	5.63
2	O K	11.04	25.63
3	F K	3.15	6.17
4	V K	82.08	59.91
5	AlK	1.92	2.64

Fig. 1 (a) XRD pattern measured within the range of $2\theta = 5°–80°$, (b) FTIR spectra captured within the range of 4000–500 cm^{-1}, (c) UV-Vis absorption spectrum of V_2CT_x across the range of 250–900 nm. Inset: Tauc plot estimating the optical band gap, (d) Raman spectra of V_2CT_x, (e) SEM Image and (f) EDX spectra of the as-synthesized V_2CT_x, (g) TEM image of the V_2CT_x MXene, (h) HRTEM image, (i) SAED pattern and (j) EDX-mapping analysis of the V_2CT_x MXene.

spectrum, in Fig. 2(b), shows peaks at 284.7 eV, 285.4 eV, and 288.6 eV attributed to C–C, C–O, and C=O, respectively.[26,27] The V 2p spectrum is fitted into two doublets, as shown in Fig. 2(c) wherein the peaks at 516.7 eV and 524.3 eV correspond to V $2p_{3/32}$ and V $2p_{\frac{1}{2}}$, respectively.[28] Moreover, three peaks at 530.9, 531.8, and 533.1 eV were found in the O 1s region, as depicted in Fig. 2(d), which can be ascribed to vanadium bonded to oxygen in varied oxidation states in V^{4+}–O/V^{5+}–O and adsorbed water, respectively.[29] The F 1s spectrum in Fig. 2(e) has been deconvoluted into two distinct peaks: one at 684.9 eV, attributed to fluorine bonded to vanadium, and a smaller peak at 686.7 eV, corresponding to residual C–F

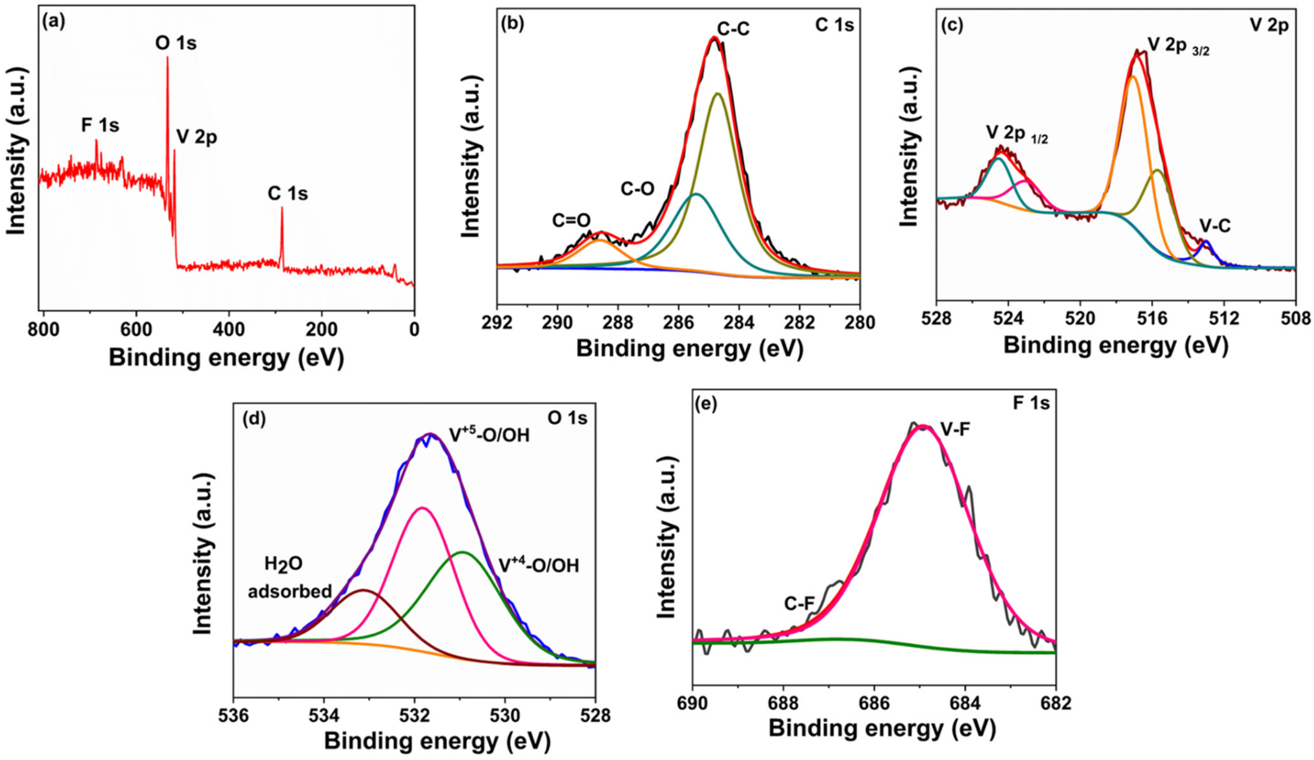

Fig. 2 XPS analysis of the V_2CT_x MXene: (a) total survey, (b) C 1s, (c) V 2p, (d) O 1s, and (e) F 1s spectra.

bonds.[26,30] All these findings demonstrated that the 2D V_2CT_x MXene was successfully synthesized using the HF/HCl mixture as an etching agent.

Voltammetric analysis

The attachment of aptamer strands onto the electrode surface, coated with the V_2CT_x MXene, was achieved through a single-step process. This resulted in hydrogen bonding interactions involving the bonding of –NH groups of the aptamer strands and the hydroxyl (OH) groups on the surface of the V_2CT_x. Hydrogen bonding, a non-covalent interaction, happens when an electronegative atom interacts with a hydrogen atom co-valently bound to another electronegative atom, such as nitrogen (NH) or oxygen (OH). In this perspective, the NH groups on the aptamer strands acted as hydrogen bond acceptors, while the OH groups on the nanohybrid surface functioned as hydrogen bond donors. During the immobilization process, stable hydrogen bonds formed between these two components as the OH groups on the nanohybrid interacted with the NH groups of the aptamer strands. This interaction effectively anchored the aptamer strands to the nanohybrid surface, ensuring immobilization.

This procedure significantly enhances the ease and efficiency of functionalizing the nanohybrid with the desired aptamer strands, paving the way for developing bioanalytical or biomedical applications that leverage versatile and efficient nanohybrids. The response analysis throughout various stages of sensor fabrication was conducted using Cyclic Voltammetry (CV), as depicted in Fig. 3(a). A substantial decrease in peak anodic current (I_{pa}) was observed when carbon screen-printed electrodes were coated with the V_2CT_x MXene. This decrease in current, from approximately 9.3 μA to 4.6 μA, can be ascribed to the interaction of Methylene Blue (MB) with the negatively charged functional groups on the vanadium MXene. MB, which contains an electron-rich benzene ring fused to a heterocyclic ring, interacts with these functional groups, thereby reducing the interface current.[31] To further confirm the decrease in current, we conducted an 8-hour absorption experiment, where the vanadium MXene absorbed methylene blue (MB). This absorption is likely attributed to hydroxyl groups and active sites on its surface. The corresponding figure is provided in the ESI.† However, after immobilizing the HER-2-specific aptamer onto the V_2CT_x-coated nano-bioelectrodes, the I_{pa} increased to approximately 33 μA. This increase is primarily due to the groove-binding interaction between the MB redox probe and the single-stranded aptamers, facilitating efficient interfacial electron transfer.[11] The unique behaviour noted at the individual phase of electrode fabrication underscores the successful development of a CSPE/V_2CT_x/Aptamer bio-nanoelectrode. The notable potential of this electrode in detecting and analyzing breast cancer illustrates the evolution in bio-nanoelectrode technology and its promising applications in medical diagnostics.

The electroactive surface of the aptasensor was assessed by examining the fluctuations in current at multiple scan speeds (varying within 20 to 100 mV s^{-1}). The associated cyclic voltammetry (CV) plots can be seen in Fig. 3(b). The current profiles exhibit reversible kinetics as the scan speed increases

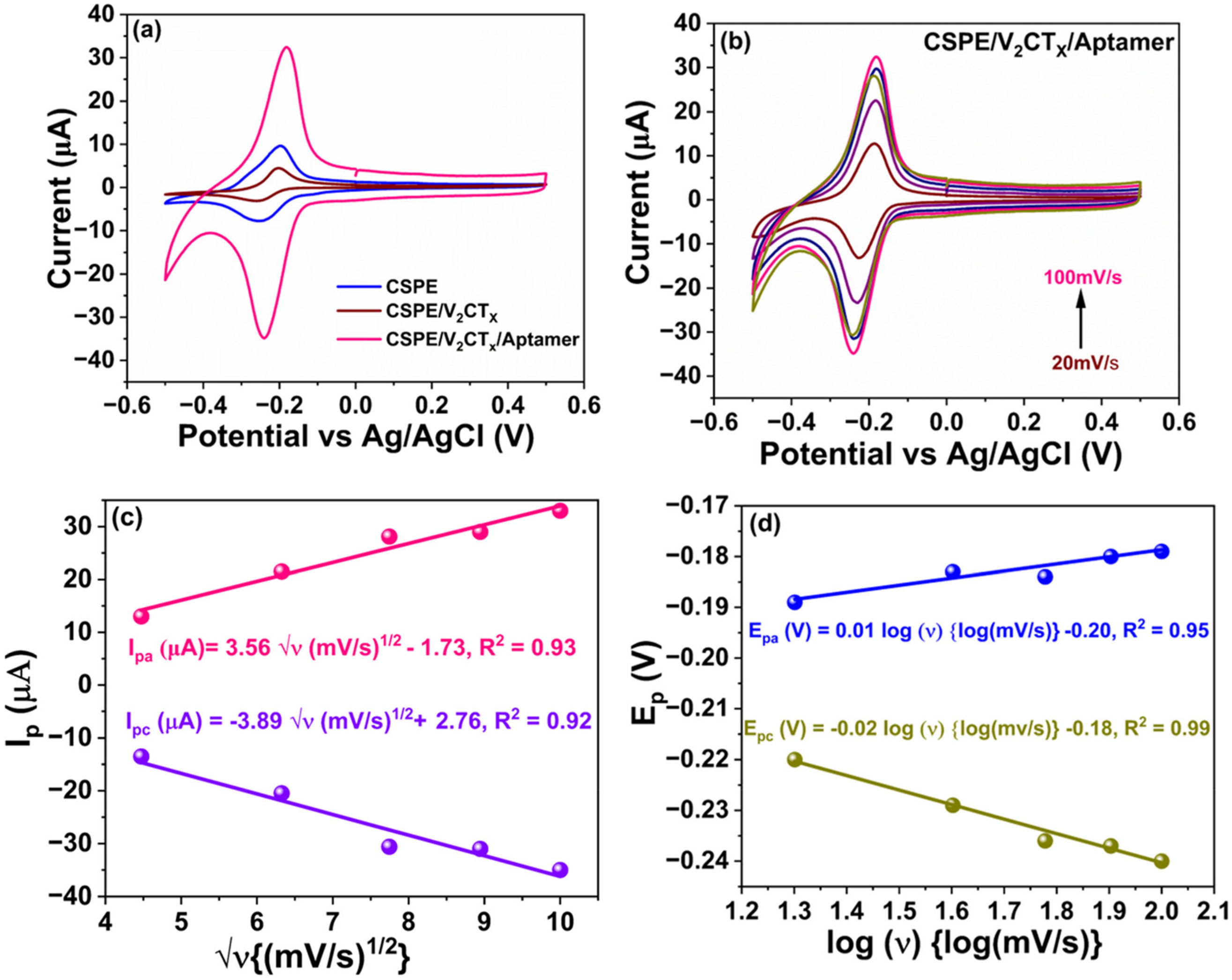

Fig. 3 (a) Cyclic voltammetric response within the potential range of −0.5 to +0.5 V in phosphate-buffered saline/methylene blue at a concentration of 0.1 M/1 µM, pH 7, comparing pristine carbon, V_2CT_x (2D) and aptamer-coated electrode surfaces. (b) Impact of scan rate on interface current at CSPE/V_2CT_x/aptamer, (c) correlation between the variation of peak current and the square root of scan rate at CSPE/V_2CT_x/aptamer, and (d) impact of scan rate on the redox peak potentials of CSPE/V_2CT_x/aptamer nanoelectrodes.

from 20 mV s^{-1} to 100 mV s^{-1}, as evidenced by the ratio of I_{pa} to I_{pc} being approximately equal to 1. The peak currents depicted in Fig. 3(c) show a linear correlation with the half-power of the scan speed, indicating diffusion-controlled kinetics and resembling a typical Randles–Sevcik behaviour.

The electroactive surface region of the sensor electrode was measured to be ~0.149 mm^2 using the Randles–Sevcik equation.[32] Such a high electroactive area of the electrode indicates a successful modification of the electrode surface, which is expected to exhibit ultrasensitive quantification of HER-2 biomarker.

The increased electroactive surface area of the CSPE/V_2CT_x/Aptamer sensing electrode significantly enhanced the overall interface current response, providing sufficient region for allowing the hybridization event. In addition, the Laviron plot[33] in Fig. 3(d) demonstrates a change in peak potentials as the scan speed varies from 20 to 100 mV s^{-1}.

The equations below demonstrate a linear correlation between the logarithm of the scan speed ($\log \nu$) and the peak potentials (E_{pa} and E_{pc}).

$$E_{pa} = 0.01\log(\nu) - 0.20, \quad R^2 = 0.98 \tag{1}$$

$$E_{pc} = -0.02\log(\nu) - 0.18, \quad R^2 = 0.96 \tag{2}$$

By conducting a comparison between these equations with the Laviron relations,[34] we obtain

$$0.01 = \frac{2.303RT}{(1-\alpha)nF} \tag{3}$$

$$-0.02 = \frac{-2.303RT}{\alpha nF} \tag{4}$$

where the number of electrons transferred is symbolised as "n". The ideal gas constant "R" is 8.314 J K^{-1} mol^{-1} and is related to thermodynamic calculations. Temperature, represented in Kelvin, affects reaction kinetics and equilibrium. Faraday's constant "F", equal to 96 500 C mol^{-1}, indicates the charge per mole of electrons. Lastly, the charge transfer coefficient "α" is a dimensionless value that signifies the energy barrier's symmetry for charge transfer, influencing reaction rates and mechanisms.

The high electroactive surface area (0.149 mm^2) and the average value of 'α' for CSPE/V_2CT_x Aptamer electrodes (0.98) are indications of an elevated degree of electron transfer, which enhances the response time of the developed sensor.

Optimization of sensing parameters

Before recording the analytical response, the sensor's performance was optimized. As shown in Fig. 4, this optimization involved adjusting the target aptamer concentration, pH level, and incubation time using Square Wave Voltammetry (SWV). Initially, the optimal target aptamer concentration was determined by monitoring changes in the anodic peak current (I_{pa}) across aptamer concentrations ranging from 10 μM to 50 μM.

The anodic peak current (I_{pa}) reached approximately 15.7 μA at an aptamer concentration of 40 μM, as shown in Fig. 4(a). This improvement in electron transfer kinetics is attributed to the effective binding of free guanine residues in the aptamer with methylene blue (MB) molecules. However, when the aptamer concentration was increased beyond 40 μM, a decrease in I_{pa} was observed. This decline is likely due to steric hindrance from accumulating multiple layers of aptamers on the electrode surface.[35] Therefore, 40 μM was the optimal aptamer concentration for further analyses.

The results shown in Fig. 4(b) illustrate the investigation of the effect of pH on sensor performance, covering a range from 5 to 7.5. It was found that a pH of 7 produced the strongest current signals. A noticeable drop in signal intensity occurred whenever the pH deviated from this neutral value, whether towards acidity (below 7) or alkalinity (above 7). This finding aligns with the usual pH of human blood, approximately 7.[4] Consequently, a pH of 7 was determined to be the optimal experimental condition, correlating with the best sensor performance and the physiological relevance in biological samples. Fig. 4(c) illustrates the impact of incubation duration on the hybridization process between recombinant proteins and aptamers. The aptamer bio-nanoelectrodes CSPE/V_2CT_x were coated with 70 μL of recombinant protein at 100 μg mL^{-1} concentration. The hybridization period was varied between 1 and 5 minutes using a PBS/MB solution (0.1 M/100 μM, pH 7). The most favorable outcome occurred at 2 minutes, as indicated by a decrease in current value with longer incubation. These findings suggest that efficient hybridization into a double helix structure occurs rapidly, within 2 minutes. This incubation period is, therefore, considered optimal for assessing the analytical capabilities of the hybridization process.

HER-2 detection using CSPE/V_2CT_x/recombinant protein electrodes

The effectiveness of the nano-bioelectrode in detecting the HER-2 recombinant protein was evaluated using square wave voltammetry (SWV) with a scan speed of 100 mV s^{-1} and a frequency of 20 Hz, within a potential span of −0.6 V to +0.1 V. The experiment utilized a PBS-MB (Phosphate-Buffered Saline-Methylene Blue) electrolyte solution with a concentration of 0.1 M/100 μM and a pH of 7. The square wave voltammetric (SWV) profiles are depicted in Fig. 5(a). An increase in the concentration of HER-2 recombinant protein from 1 ng mL^{-1} to 100 μg mL^{-1} resulted in a decrease in the peak anodic current (I_{pa}). when the amounts of recombinant proteins were raised, the redox process of MB, crucial for electron transport, was significantly hindered. The formation of larger hybridized complexes on the electrode surface impedes the electron flow channel. During DNA hybridization, these significant complexes create a physical barrier that obstructs effective electron transport, leading to reduced electrochemical activity and impacting the overall performance of the electrode.[36] Notably, the electrochemical reactions mediated by the MB probe maintain their reversibility, as evidenced by the minimal changes in peak potentials and the consistent I_{pa}/I_{pc} ratio of approximately 1. This finding underscores the electrochemical stability of the sensor platform during binding events within the required electrochemical range.

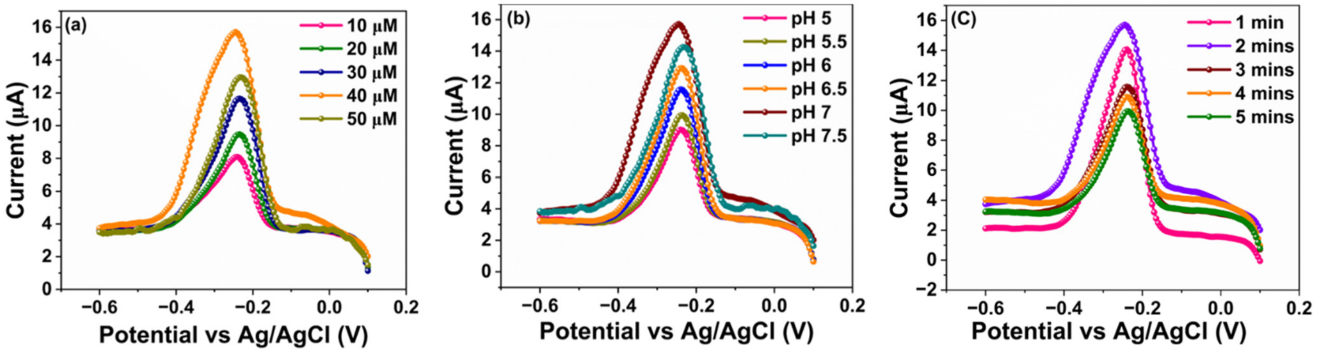

Fig. 4 Square wave voltammograms (SWV) obtained at (a) different HER-2 aptamer concentrations, (b) effect of varying pH levels within the range of 5 to 7.5 on the hybridization of 100 μM recombinant protein, and (c) influence of incubation time on the response of 100 μM HER-2 recombinant protein.

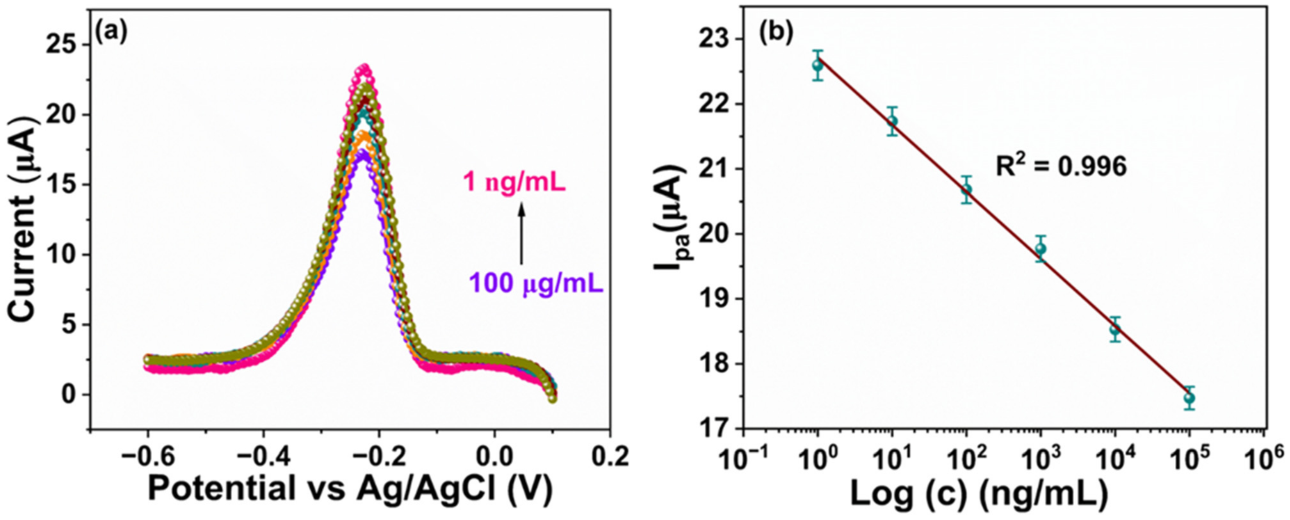

Fig. 5 (a) Square wave voltammetric profiles at various concentrations of the recombinant HER-2 protein ranging from 1 ng mL^{-1} to 100 µg mL^{-1}. (b) Sensor calibration graph was achieved at 0.22 V (−220 mV), showing a linear correlation between the peak current (I_{pa}) and the HER-2 recombinant protein concentrations.

The CSPE/V_2CT_x/Aptasensor was calibrated at the anodic potential of −220 mV. Fig. 5(b) demonstrates an inverse correlation between the concentration of HER-2 recombinant protein and I_{pa}. As the concentration of HER-2 was increased from 1 ng mL^{-1} to 100 µg mL^{-1}, the current decreased from approximately 23.2 µA to 17.1 µA. This decrease in I_{pa} is primarily due to the formation of macromolecular complexes during DNA hybridization, which obstructs the interface electron transfer.[37]

$$\log\{I_{\text{pa}}(\mu\text{A})\} = -1.03195\log\{c(\text{ng mL}^{-1})\} + 22.71 \quad (R^2 = 0.996) \tag{5}$$

The data strongly correlates with the linear model, indicating a robust fit as indicated in eqn (5). The biosensor exhibited a 6.93 µA ng^{-1} mL^{-1} mm^{-2} sensitivity. The detection threshold (LoD) and limit of quantification (LoQ) were evaluated based on the 3-sigma and 10-sigma rules (eqn (6) and (7)), respectively.[38]

$$\text{LOD} = (3.3 \times 0.11307) \div 1.03195 = 0.36 \text{ ng mL}^{-1} \tag{6}$$

where sigma σ is the standard deviation of the blank signal, and S is the slope of the calibration curve. This approach ensures that the LoD represents the lowest concentration of HER-2 recombinant protein that can be reliably detected with a signal distinguishable from the background noise.

$$\text{LOQ} = (10 \times 0.11307) \div 1.03195 = 1.09 \text{ ng mL}^{-1} \tag{7}$$

The LoQ represents the minimum concentration of HER-2 that can be quantified accurately and precisely. The LoQ provides a higher confidence level than the LoD, making it suitable for quantification purposes in analytical applications (Table 1).

Selectivity and shelf-life studies

To verify the specificity of the HER-2 sensor, its performance was evaluated in the presence of various other analytes. The analytes added individually to the detection solution included Covid-19 (1 ng mL^{-1}) and PCA-3 (1 ng mL^{-1}). The tests were carried out under ideal circumstances, specifically utilizing phosphate-buffered saline/methylene blue at a concentration of 0.1 M/100 µM, pH 7. According to the results, the peak current was largest when HER-2 was present, as depicted in Fig. 6(a). This suggests that the aptasensing platform created has strong selectivity towards the HER-2 recombinant protein and does not interact with other analytes. Furthermore, its shelf life was observed to check its stability, as depicted in Fig. 6(b). The stable nature of the sensor platform was

Table 1 Comparison of sensing parameters with those reported in the previous studies

S. no.	Surface enhancer	Linear measurement span	Detection threshold	Ref.
1	LSG-AuNS-MIP	1 ng mL^{-1} to 200 ng mL^{-1}	0.43 ng mL^{-1}	39
2	Graphene oxide	0.5 ng mL^{-1} to 25 ng mL^{-1}	0.59 ng mL^{-1}	40
3	MIP/AuSPE	10 ng mL^{-1} to 70 ng mL^{-1}	1.6 ng mL^{-1}	41
4	SPE/poly-L-lysine	10 ng ml^{-1} to 60 ng ml^{-1}	3.0 ng mL^{-1}	42
5	SPCE/CdSe@ZnS	10 ng mL^{-1} to 150 ng mL^{-1}	2.1 ng mL^{-1}	43
6	**CSPE-V_2CT_x**	**1 ng mL^{-1} to 100 µg mL^{-1}**	**0.36 ng mL^{-1}**	**Present work**

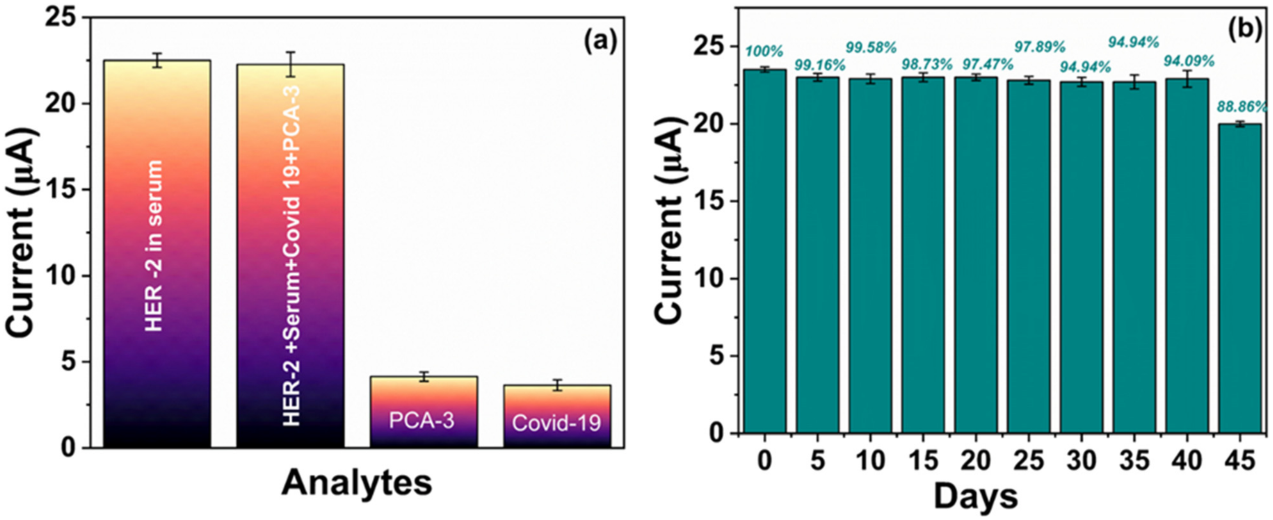

Fig. 6 (a) Inference analysis of the HER-2 aptasensor in the presence of various analytes. (b) Shelf-life evaluation of the developed sensor over 40 days.

observed for 40 days. After 40 days, the current response was slightly decreased.

Conclusion

In this study, we developed an ultrasensitive electrochemical aptasensor for the early diagnosis of HER-2, leveraging the V_2CT_x MXene as the sensing platform. The aptasensor demonstrated an impressive linear detection range of 1 ng mL^{-1} to 100 μg mL^{-1}, providing versatility for detecting HER-2 across a wide range of concentrations. It achieved a detection limit (LOD) of 0.36 ng mL^{-1}, a limit of quantification (LOQ) of 1.09 ng mL^{-1}, and a remarkable sensitivity of 6.93 μA ng^{-1} mL^{-1} mm^{-2}, enabling the identification and precise quantification of HER-2, which is critical for early breast cancer diagnosis. The sensor exhibited excellent stability, retaining its performance for up to 40 days under optimized conditions, making it suitable for prolonged use in healthcare applications. Furthermore, the aptasensor demonstrated high selectivity for HER-2, effectively minimizing interference from other biomarkers and ensuring reliable and accurate detection. These findings highlight the potential of this platform as a cost-effective, non-invasive diagnostic tool for early breast cancer detection. Its rapid response, high sensitivity, and excellent stability could significantly improve patient monitoring and clinical outcomes for breast cancer management. This study represents a significant step in utilizing MXene-based materials for advanced biosensing applications.

Author contributions

Reema Rawat: investigation, data curation, formal analysis, validation, and writing – original draft. Sonam Singh: investigation, writing – original draft, and formal analysis. Souradeep Roy: review and editing. Samarika Dubey: investigation. Tapas Goswami: visualization, supervision, project administration, and funding acquisition. Ashish Mathur: visualization, supervision, project administration, and funding acquisition. James McLaughlin: review and editing.

Data availability

Data will be made available on reasonable request.

Conflicts of interest

The authors declare no competing interests.

Acknowledgements

The authors would like to acknowledge the Indo-ASEAN grant [CRD/2021/000472] and UPES SEED infrastructure grant [UPES/R&D-SEED-INFRA/11032022/01]. The authors would also like to thank the Central Instrumentation Centre [CIC] at UPES, Dehradun [India] and the electron beamline facilities at Suranaree University of Technology [Thailand] for assisting in this research.

References

1 J. G. Pacheco, P. Rebelo, M. Freitas, H. P. A. Nouws and C. Delerue-Matos, *Sens. Actuators, B*, 2018, **273**, 1008–1014.
2 P. Lakhera, V. Chaudhary, A. Jha, R. Singh, P. Kush and P. Kumar, Elsevier Ltd, 2022, preprint, DOI: 10.1016/j.mtchem.2022.101129.

3 L. Chun, S. E. Kim, M. Cho, W. S. Choe, J. Nam, D. W. Lee and Y. Lee, *Sens. Actuators, B*, 2013, **186**, 446–450.

4 S. Yang, M. You, F. Zhang, Q. Wang and P. He, *Sens. Actuators, B*, 2018, **258**, 796–802.

5 Q. Zhang, R. Ma, Y. Zhang, J. Zhao, Y. Wang and Z. Xu, *ACS Sens.*, 2023, **8**, 875–883.

6 M. Sadeghi, S. Kashanian, S. M. Naghib, F. Haghiralsadat and D. Tofighi, *Int. J. Electrochem. Sci.*, 2022, **17**(4), 220459–220473.

7 P. Sarkar, K. N. Huffman, T. Williams, A. Deol, I. Zorra, T. Adam, R. Donaldson, U. Qureshi, K. Gowda and R. D. Galiano, John Wiley and Sons Inc., 2024, preprint, DOI: 10.1002/jso.27584.

8 M. Faridi, F. L. Kashani and S. Vaziri, *Iran. J. Breast. Dis.*, 2024, **16**, 50–68.

9 S. Nagabooshanam, S. Roy, A. Mathur, I. Mukherjee, S. Krishnamurthy and L. M. Bharadwaj, *Sci. Rep.*, 2019, **9**, 19862–19870.

10 C. Singhal, C. S. Pundir and J. Narang, *Biosens. Bioelectron.*, 2017, **97**, 75–82.

11 R. Rawat, S. Singh, S. Roy, A. Kumar, T. Goswami and A. Mathur, *Mater. Chem. Phys.*, 2023, **295**, 127050–127057.

12 R. Rawat, S. Roy, T. Goswami and A. Mathur, *Diagnostics*, 2022, **12**(9), 2087–2097.

13 T. Yu, S. Li, L. Zhang, F. Li, J. Wang, H. Pan and D. Zhang, *J. Colloid Interface Sci.*, 2023, **629**, 546–558.

14 M. Rethinasabapathy, D. Dhiman, K. S. Ranjith, S.-K. Hwang, Y. S. Huh and P. Venkatesu, *Appl. Surf. Sci.*, 2024, 160108.

15 M. P. Bilibana, *Adv. Sens. Energy Mater.*, 2023, **2**, 100080.

16 H. Kim and H. N. Alshareef, American Chemical Society, 2020, preprint, DOI: 10.1021/acsmaterialslett.9b00419.

17 W. Feng, H. Luo, Y. Wang, S. Zeng, L. Deng, X. Zhou, H. Zhang and S. Peng, *RSC Adv.*, 2018, **8**, 2398–2403.

18 K. Allen-Perry, W. Straka, D. Keith, S. Han, L. Reynolds, B. Gautam and D. E. Autrey, *Materials*, 2021, **14**, 1–9.

19 P. Ridley, C. Gallano, R. Andris, C. E. Shuck, Y. Gogotsi and E. Pomerantseva, *ACS Appl. Energy Mater.*, 2020, **3**, 10892–10901.

20 S. M. Majhi, A. Ali, Y. E. Greish, H. F. El-Maghraby and S. T. Mahmoud, *Sci. Rep.*, 2023, **13**, 3114–3125.

21 R. Thakur, A. Vahidmohammadi, J. Moncada, W. R. Adams, M. Chi, B. Tatarchuk, M. Beidaghi and C. A. Carrero, *Nanoscale*, 2019, **11**, 10716–10726.

22 E. Lee, A. Vahidmohammadi, Y. S. Yoon, M. Beidaghi and D. J. Kim, *ACS Sens.*, 2019, **4**, 1603–1611.

23 M. S. Mohseni-Salehi, E. Taheri-Nassaj, A. Babaei, A. S. Ghazvini and M. Soleimanzade, *J. Energy Storage*, 2023, **66**, 107462–107475.

24 B. Wang, A. Zhou, F. Liu, J. Cao, L. Wang and Q. Hu, *J. Adv. Ceram.*, 2018, **7**, 237–245.

25 K. Y. Lau, *Recent advances of MXene saturable absorber for near-infrared mode-locked fiber laser*, 2021, 2109–13011.

26 E. Lee, A. Vahidmohammadi, Y. S. Yoon, M. Beidaghi and D. J. Kim, *ACS Sens.*, 2019, **4**, 1603–1611.

27 S. Young Kwon, J. Lee, Y. I. Jhon, G. Lim, Y. M. Jhon and J. H. Lee, *Opt. Mater.*, 2022, **134**, 113198–113204.

28 J. Xia, H. Guo, G. Yu, Q. Chen, Y. Liu, Q. Liu, Y. Luo, T. Li and E. Traversa, *Catal. Lett.*, 2021, **151**, 3516–3522.

29 S. M. Majhi, A. Ali, Y. E. Greish, H. F. El-Maghraby and S. T. Mahmoud, *Sci. Rep.*, 2023, **13**, 3114–3125.

30 N. Mahar, A. Al-Ahmed and A. A. Al-Saadi, *Appl. Surf. Sci.*, 2023, **607**, 155034–155043.

31 H. Lei, Z. Hao, K. Chen, K. Chen, Y. Chen, J. Zhang, Z. Hu, Y. Song, P. Rao, Q. Huang and Q. Huang, *J. Phys. Chem. Lett.*, 2020, **11**, 4253–4260.

32 P. Szroeder, N. G. Tsierkezos, M. Walczyk, W. Strupiński, A. Górska-Pukownik, J. Strzelecki, K. Wiwatowski, P. Scharff and U. Ritter, *J. Solid State Electrochem.*, 2014, **18**, 2555–2562.

33 S. Roy, S. Singh, M. Khan, E. Chamanehpour, S. Sain, T. Goswami, S. S. Roy, Y. K. Mishra and A. Mathur, *Electrochim. Acta*, 2024, **477**, 143762–143770.

34 Y. Tang, S. Zheng, Y. Xu, X. Xiao, H. Xue and H. Pang, Elsevier B.V., 2018, preprint, DOI: 10.1016/j.ensm.2018.02.010.

35 L. Gao, C. Lian, Y. Zhou, L. Yan, Q. Li, C. Zhang, L. Chen and K. Chen, Elsevier Ltd, 2014, preprint, DOI: 10.1016/j.bios.2014.03.039.

36 F. Jia, N. Duan, S. Wu, X. Ma, Y. Xia, Z. Wang and X. Wei, *Microchim. Acta*, 2014, **181**, 967–974.

37 C. Singhal, M. Khanuja, N. Chaudhary, C. S. Pundir and J. Narang, *Sci. Rep.*, 2018, **8**, 7734–7744.

38 A. X. Ding, Y. Di Shi, K. X. Zhang, W. Sun, Z. L. Tan, Z. L. Lu and L. He, *Sens. Actuators, B*, 2018, **255**, 440–447.

39 S. Rauf, A. A. Lahcen, A. Aljedaibi, T. Beduk, J. Ilton de Oliveira Filho and K. N. Salama, *Biosens. Bioelectron.*, 2021, **180**, 113116–113123.

40 M. Sadeghi, S. Kashanian, S. M. Naghib, F. Haghiralsadat and D. Tofighi, *Int. J. Electrochem. Sci.*, 2022, **17**(4), 220459–220473.

41 J. G. Pacheco, P. Rebelo, M. Freitas, H. P. A. Nouws and C. Delerue-Matos, *Sens. Actuators, B*, 2018, **273**, 1008–1014.

42 G. Bezerra, C. Córdula, D. Campos, G. Nascimento, N. Oliveira, M. A. Seabra, V. Visani, S. Lucas, I. Lopes, J. Santos, F. Xavier, M. A. Borba, D. Martins and J. Lima-Filho, *Anal. Bioanal. Chem.*, 2019, **411**, 6667–6676.

43 M. Freitas, M. M. P. S. Neves, H. P. A. Nouws and C. Delerue-Matos, *Talanta*, 2020, **208**, 120430–120437.